

Investigation of Reflection-Based Measurements of Microwave Kinetic Inductance Detectors in the Optical Bands

Jie Hu^{1,2}, Faouzi Boussaha¹, Paul Nicaise¹, Christine Chaumont¹, Maria Appavou¹, Viet Dung Pham² and Michel Piat²

¹GEPI, Observatoire de Paris, PSL Université, CNRS, 75014 Paris, France

²Université de Paris, CNRS, Astroparticule et Cosmologie, F-75013 Paris, France

(*Authors to whom correspondence should be addressed: jie.hu@obspm.fr)

(Dated: 17 June 2024)

In this paper, we investigate the single photon response from the reflection of the Microwave Kinetic Inductance Detector (MKID) array. Reflection measurements are carried out using two configurations: one is measured simultaneously with the transmission, and the other is obtained with a single-ended MKID array terminated with an open load. Compared with the transmission, reflection measurements significantly reduce the readout noise of the single-ended MKID array. This is also reflected in the improvement of the median energy resolving power by around 20-30% under pulsed photon illumination at $\lambda = 405$ nm, mainly due to an increase in the size of the resonance circle on the IQ plane. This method has the potential to be used to read out large MKID arrays.

The Microwave Kinetic Inductance Detector¹ (MKID) has emerged as a groundbreaking technology with wide-ranging applications in astrophysics, spanning from millimeter-wave² and optical^{3,4} to X-ray observations⁵ for its wideband operation, intrinsic frequency domain multiplexity and relatively simple fabrication. In the optical and near-infrared bands, MKIDs demonstrate a distinctive blend of excellent energy resolution and the ease of scalability into large arrays⁶⁻⁹, providing a significant advantage in applications like extreme faint object detection and low-resolution spectroscopy like SPIAKID⁴.

MKIDs typically consist of high-quality lumped superconducting resonators in the optical and near-infrared bands. These resonators, as discussed in⁸⁻¹², are constructed with an interdigitated capacitor (IDC) and a meander inductor. When photons with energies $h\nu > 2\Delta$ (2Δ the Cooper pair binding energy) are absorbed in the meander, they generate phonons, disrupt Cooper pairs, and produce quasiparticles (QPs). These additional QPs increase the kinetic inductance, lowering the resonator's resonance frequency and quality factor. This response can be detected through changes in the phase and amplitude of the resonator, respectively, by applying a probing tone at the resonance frequency.

The performance of optical MKIDs is characterized by their energy-resolving power R , which currently faces domination by three distinct noise sources. The first is the noise caused by the escape of hot phonons from the meander to the substrate, as discussed in the literature^{8,9}. The second is the two-level system noise (TLS) generated within the substrate and at the superconductor/substrate interface¹³. The last is the readout noise from the system, primarily stemming from the low noise amplifier (LNA), which plays a significant role. Efforts have been dedicated to reducing this readout noise, notably through implementing superconducting parametric amplifiers^{9,14}, which are still not commercially available for reading out MKIDs.

Presently, MKIDs are typically read out via the transmission of the resonator. However, due to the inherent nature of MKIDs, strong reflections can occur at resonance, especially

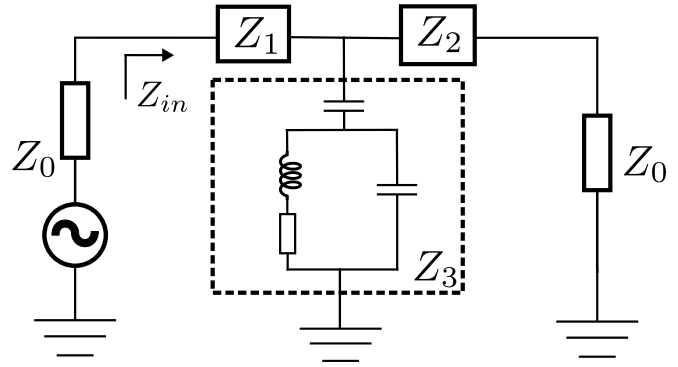


FIG. 1. MKIDs T-junction circuit

in the case of high-quality superconducting resonators where the reflected signal (S_{11}) can surpass the transmitted signal (S_{21}). Consequently, by utilizing S_{11} for resonator readout, there is potential to diminish the sensitivity of the resonator to readout noise within the system. This signal, however, is not traditionally measured in the conventional homodyne configuration.

In this paper, we investigate the single-photon response of TiN/Ti/TiN MKIDs⁴ measured by reflection. To capture the reflected signal, a cryogenic circulator is positioned at the input of the MKID array, with the reflected signal (S_{11}) read from the circulator's third port—a methodology commonly employed for qubit readout.^{15,16} Two distinct configurations are compared. In the first configuration, both S_{11} and S_{21} , taken as a reference, are measured simultaneously. In contrast, only S_{11} is measured in the second configuration when the MKID array is terminated with an open load. The latter is referred to as single-ended MKIDs. Across all configurations, we observed a single-photon response, with the single-ended MKID array demonstrating the most favorable median R , approximately 20-30%

The equivalent circuit of the MKID shunted-coupled to a transmission line with a characteristic impedance Z_0 can be generally represented in Fig. 1. Z_1 and Z_2 are general de-

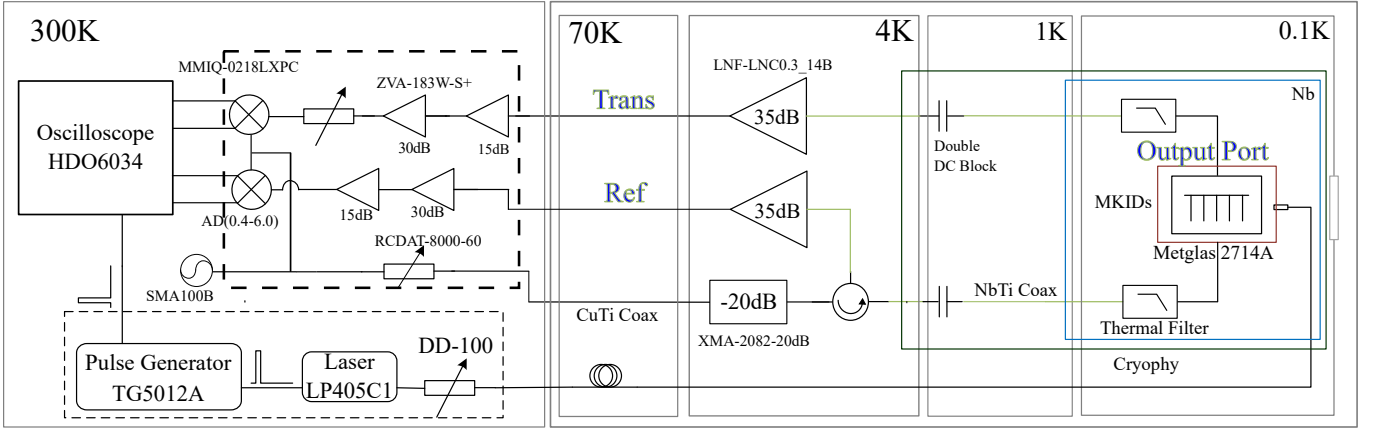


FIG. 2. Measurement Setup with reflection (S_{11}) and transmission (S_{21}). The S_{11} -open is obtained by terminating the output port of the MKIDs with an open load. The reflected signal is obtained by putting an isolator at the input of the resonator. The isolator is currently placed on the 4K stage due to the limited space on the 0.1K stage.

descriptions of the port impedance, which can either be the impedance mismatch or the impedance of the transmission lines. Z_3 is the MKID impedance. S_{11} can be obtained as

$$S_{11} = \frac{AZ_3 + \Gamma_0}{1 + 2Z_3/\hat{Z}_0} \quad (1)$$

with

$$\hat{Z}_0 = \frac{2(Z_1 + Z_0)(Z_2 + Z_0)}{2Z_0 + Z_1 + Z_2} \quad (2)$$

$$A = \frac{Z_1 + Z_2}{(Z_0 + Z_1)(Z_0 + Z_2)} \quad (3)$$

$$\Gamma_0 = \frac{Z_1 - Z_0}{Z_1 + Z_0} \quad (4)$$

\hat{Z}_0 and Γ_0 are the equivalent characteristic impedance of the transmission line and the reflection coefficient at the MKID array input. S_{21} of the MKIDs can be expressed as⁹

$$S_{21} = \frac{2Z_0}{2Z_0 + Z_1 + Z_2} \left(1 - \frac{1}{1 + 2Z_3/\hat{Z}_0}\right) \quad (5)$$

with^{9,17}

$$\frac{1}{1 + 2Z_3/\hat{Z}_0} = \frac{Q/Q_c - 2jQx_a}{1 + 2jQx_g} \quad (6)$$

where Q and Q_c are, respectively, the quality factor and the coupling quality factor of the resonator, $x_g = (f - f_r)/f_r$ is the detuning of the generator frequency from resonance, and $x_a = \delta f_a/f_r$ is the fractional detuning of the original resonance frequency due to the impedance mismatches. By substituting Eq. (6) into Eq. (A),

$$S_{11} = \gamma - (\gamma - \Gamma_0) \frac{Q/Q_c - 2jQx_a}{1 + 2jQx_g} \quad (7)$$

Then, S_{11} can be fitted with

$$S_{11} = (\gamma - \Gamma_0) \left(\gamma_0 - \frac{Q/Q_c - 2jQx_a}{1 + 2jQx_g} \right) \quad (8)$$

with $\gamma_0 = \gamma/(\gamma - \Gamma_0)$ and $\gamma = (Z_1 + Z_2)/(2Z_0 + Z_1 + Z_2)$ as a complex fitting parameter. The amplitude of S_{11} and the location of its center of the resonance circle in the IQ plane will depend on the value of γ_0 . For a matched resonator, i.e. $Z_1 = Z_2 \rightarrow 0$, $\gamma_0 \rightarrow 0$. S_{11} will show a maximum at the resonance frequency. When $Z_2 \rightarrow \infty$ and $Z_1 \rightarrow 0$, $\gamma_0 \rightarrow 1/2$, the magnitude of S_{11} will be similar to S_{21} and shows a minimum at the resonance. A more detailed mathematical procedure for Eq. (S12) can be found in Appendix A.

The detailed measurement setup for the MKIDs is illustrated in Fig. 2. The MKIDs undergo characterization within a pre-cooled two-stage pulse tube Adiabatic Demagnetization Refrigerator (ADR). A 1.5mm-thick niobium cylinder, sheets of metglas 2714a surrounding the MKIDs, and a 2mm-thick cylinder of Cryophy are employed on the 4K stage to shield from magnetic interference. Each MKID is individually read out using a standard homodyne mixing scheme.

The input signal, generated by a signal generator, is attenuated by a programmable attenuator at room temperature and a 20 dB attenuator at 4 K. A circulator is positioned at the input of the MKIDs to capture the S_{11} signal. Due to space limitations on the 100 mK stage, attenuators on the 1 K and 100 mK stages are temporarily removed to acquire the S_{11} signal. The thermal noise above 100 GHz is well-attenuated thanks to the thermal filters on the 100 mK stage. Thus, the background noise at the MKIDs should remain low¹⁸, although the thermal noise at the resonance frequency band remains. It should also be noted that placing the circulator on the 100 mK stage will reduce the system noise, thus further improving R.

The transmitted and reflected signals from MKIDs are initially amplified by an LNA on the 4 K stage and further amplified by two room-temperature amplifiers. Subsequently, the transmitted and reflected signals are down-converted to DC by two IQ mixers and then sampled by an oscilloscope. The readout power at the detector's input is estimated to be approximately -100 dBm.

Illumination of the MKIDs array is achieved through an optical fiber positioned 35 mm above the pixels. A 405 nm laser,

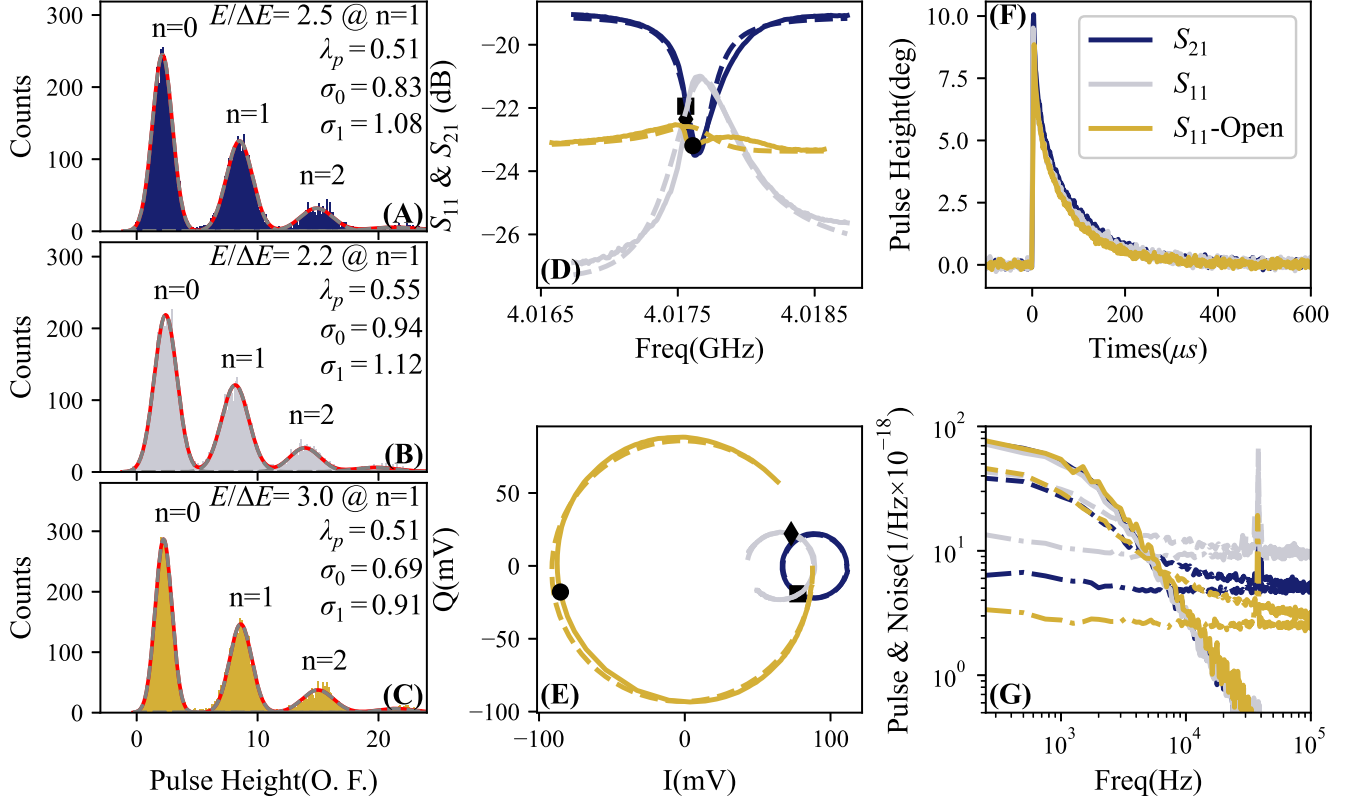


FIG. 3. Comparison of the single-photon response of the MKID at 4.018 GHz from the transmission and reflection at $T_{bath} = 200$ mK (A)-(C): Measured pulse statistics from S_{21} , S_{11} and S_{11} -Open. λ_p is the fitted mean value of the Poisson distribution. σ_0 and σ_1 are the standard deviations of the first and second peaks. (D)-(E): Comparison of the amplitude of the MKID and its trajectory on the IQ plane. The black dots indicate the readout frequency. The dashed lines are the fitted curves with Eq. (S7) and (S12). (F): The averaged single-photon response with hundreds of pulse events with $n = 1$ as shown in (A)-(C). (G): Comparison between the noise spectrum and the pulse shown in (F), obtained by Fourier transformation. The dashed line (---) is the noise in phase, and the dash-dot line (-·-) is the noise in amplitude.

modulated by a 250 Hz pulse from a pulse generator with a width of around 50 ns, is employed for illumination. The laser output power is adjusted outside the cryostat using a digital step attenuator. The pulse response of the MKID is sampled by an oscilloscope at a frequency of 5-10 MHz.

Two different configurations are employed for the measurement of the MKIDs. First, S_{11} and S_{21} are measured simultaneously. Second, the responses of the MKIDs terminated with an open load at the output port of the array are measured, as depicted in Fig. 2, and the corresponding result is labeled as S_{11} -open.

Our array comprises 30×30 MKIDs. Each MKID consists of a 10 nm/10 nm/10 nm-thick TiN/Ti/TiN trilayer meander connected to a niobium capacitor. The meander size is $36 \times 36 \mu\text{m}^2$. The measured critical temperature T_c of the trilayer film is around 1.75 K. A more detailed description of the design of the pixels can be found in our previous publication⁴.

As depicted in Fig.3, we first conducted a comparison of the measured single-photon response of the MKID obtained from S_{11} , S_{21} , and S_{11} -Open. In all cases, the MKID resonating at around 4.018 GHz was measured with a readout of approximately 2 dB below saturation at the frequency showing

the maximum response on the IQ plane. Each measurement recorded around 10,000 pulse events and was processed by the standard wiener filtering⁷. The resulting pulse height statistics are illustrated in Fig.3-(A)-(C), and these data were fitted using the convolution between the Gaussian and Poisson distributions, as¹⁹.

$$p(\phi) = \sum_{n=0}^{\infty} \frac{\lambda_p^n}{n!} e^{-(\phi - n\phi_1 - \phi_0)^2 / (2\sigma_n^2)} \quad (9)$$

Here, λ_p is the mean value of the Poisson distribution, ϕ_0 is the mean value of the 0-th peak that is the background response from the chip, σ_n is the variance of the n-th peak, and ϕ_1 is the difference between the peaks, which is the response of a single photon.

Here, we consider the width of the 0-photon peak is dominated by the system noise σ_s , i.e., the two-level system (TLS) noise σ_{TLS} from the MKID itself and the readout noise σ_r .

$$\sigma_0^2 = \sigma_{TLS}^2 + \sigma_r^2, \quad (10)$$

The width of the 1-photon peak is dominated by the readout noise and the noise related from the photon absorption σ_p , i.e.,

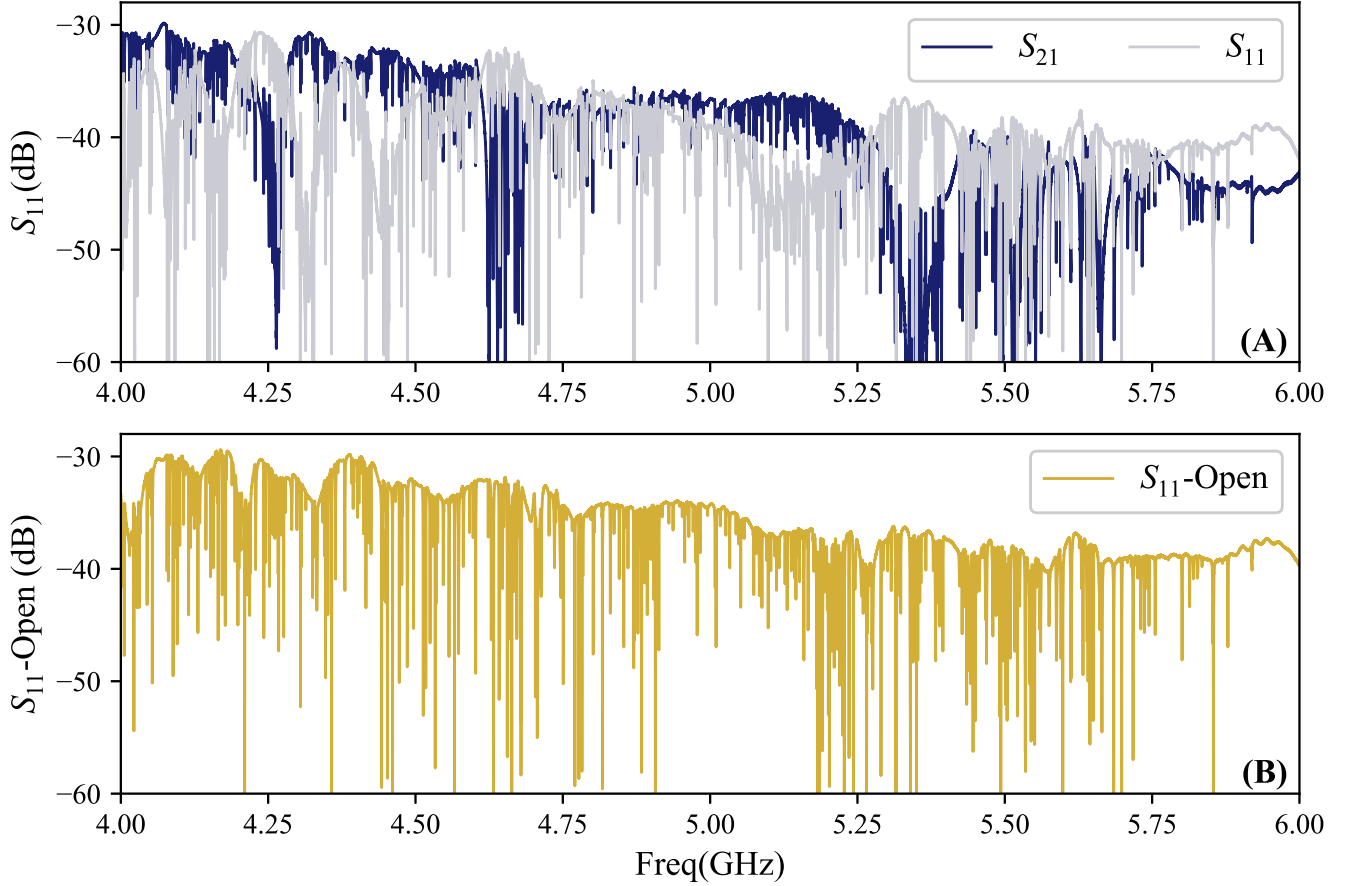


FIG. 4. (A)-(B): Comparison of amplitudes of S_{21} , S_{11} and S_{11} -Open respectively. There are two transmission zeros around 4.25 GHz and 5.35 GHz.

TABLE I. Fitted parameters and contribution of each noise to R for the resonator at 4.0175 GHz.

	Q_c (k)	Q_i (k)	γ_0	σ_{TLS} (O. F.)	σ_r (O. F.)	σ_p (O. F.)
S_{21}	32k	21k	1.0	0.61	0.56	0.61
S_{11}	25k	17k	$0.06 + 1.0j$	0.60	0.72	0.69
S_{11} -Open	16k	19k	$0.27 + 0.35j$	0.58	0.38	0.59

the hot phonon escape⁸ and the current non-uniformity in the meander¹⁴ as

$$\sigma_1^2 = \sigma_0^2 + \sigma_p^2 \quad (11)$$

Here, σ_p is dominated by the phonon escape noise. Since the TLS is mainly in the phase response of MKID, σ_r can be obtained by convolving the amplitude response in the 0-photon peak with the wiener filter. We list the contribution of each noise of the resonator at 4.0175 GHz in Table I. It can be seen that the σ_{TLS} and σ_p are consistent with each other. The difference in the R s of S_{21} , S_{11} and S_{11} -open is due to the different levels of the readout noise. The R of S_{11} -Open is dominated by the TLS and the phonon escape noise.

The increase in the readout noise in S_{11} can be attributed

to two possible reasons. First, the presence of the reflection chain especially the circulator can lead to an increase in readout noise. Second, the MKID is read out at the frequency exhibiting maximum response in the IQ plane, resulting in similar output powers at the output port of the MKID across all cases, as depicted in Fig. 3-(D)-(E), where the black dots represent the position of the readout signals. Consequently, the signal obtained from the reflection may not be significantly higher than the S_{21} 's. The dashed lines are the fitted results with Eq. (S7) and Eq. (S12) and the fitted parameters are listed in Table I, which shows the internal quality factor Q_i are in good agreement with each other. The initial values strongly influence the fitted parameters, yet their impact on estimating the pulse response is minimal.

The reduction of the readout noise in S_{11} -open is due to the increase of the radius of the resonance circle r , which is shown in Fig.3-(E). as there is no significant difference in the pulse response shown in Fig.3-(F). The readout noise is related to r as²⁰

$$S_{DSB} = \frac{k_B T_r}{r^2 P_r}, \quad (12)$$

where k_B is the Boltzmann constant T_r is the equivalent input noise temperature of the readout system. P_r is the level

of the readout power. Thus, the readout noise would be reduced when there is an increase in the radius of the resonance circle. This is also supported by the noise spectrum shown in Fig. 3-(G). Eq. (12) is qualitatively in agreement with the measurement by taking into account that the readout power of S_{11} -open is 2 dB lower than that of S_{21} . For matched resonators (i.e, $Z_1 = 0$ and $Z_2 = 0$ for the case of S_{11} and S_{21} , and $Z_1 = 0$ and $Z_2 = \infty$ for S_{11} -Open), the radius of the resonance circle of S_{11} , S_{21} and S_{11} -open can be expressed as

$$r = \begin{cases} \frac{Q_i}{2(Q_i+Q_c)} \sqrt{4(Q_c x_a)^2 + 1} & S_{11} \text{ \& } S_{21} \\ \frac{Q_i}{Q_i+Q'_c} \sqrt{4(Q'_c x_a)^2 + 1} & S_{11} - \text{Open} \end{cases} \quad (13)$$

Q_i is the internal quality factor of the resonator and $1/Q = 1/Q_c + 1/Q_i$. The coupling quality factor Q'_c of the S_{11} -Open will change due as

$$Q'_c = \frac{C}{\omega_r C_c^2} \operatorname{Re} \left\{ \frac{2Z_0 + Z_1 + Z_2}{(Z_0 + Z_1)(Z_0 + Z_2)} \right\} \quad (14)$$

where C and C_c are, respectively, the capacitors of the resonance and the coupling capacitor to the feedline. ω_r is the angular resonance frequency. Q'_c will reduce when $Z_0 + Z_2 \rightarrow \infty$, which is agreement with the Q_c fitted from the S_{21} and S_{11} -open. In this case, for a matched resonator ($x_a = 0$), the radius of the resonance circle will be increased by more than a factor of 2. A comprehensive mathematical derivation for determining the radius of the resonance circle can be found in Appendix B.

The readout scheme utilizing S_{11} -Open presents a notable advantage for systems featuring significant ripples in the baseline particularly due to the absence of bridges that balance the CPW ground²¹. In Fig. 4, we compare the amplitudes of S_{11} , S_{21} , and S_{11} -Open across the frequency range from 4.00 GHz to 6.00 GHz. Notably, where a minimum exists in S_{21} , there is a corresponding maximum in S_{11} , and vice versa. Additionally, as the frequency surpasses 5.50 GHz, the magnitude of S_{11} begins to exceed that of S_{21} , elucidating the unexpected additional reduction in the magnitude of S_{21} within our system. It can be seen that terminating the array with an open load remarkably diminishes the grounding effect to approximately ± 3 dB, a level comparable to state-of-the-art MKID arrays^{22,23}. Note the amplitude of the S_{11} and S_{11} -Open depends strongly on the γ_0 in Eq. S12, which is determined by the matching condition of the resonator to the circuit. When γ_0 is real positive, S_{11} and S_{11} -Open will have similar amplitude with S_{21} . The amplitude of S_{11} -Open shown in Fig.3 is a special case with the center of the resonance circle close to the origin of the IQ plane.

Further investigations will be performed for larger MKIDs with multiple readout lines to check if the bridges that balance the ground can be eliminated.

We conducted a comparison of the energy resolution (R) across three frequency bands: 4.19-4.29 GHz, 4.75-4.95 GHz, and 5.30-5.40 GHz, where two of them exhibit a minimum in the amplitude, as depicted in Fig. 5-(A). The measured R s within the corresponding bands are illustrated in Fig. 5-(B). Despite the amplitude of S_{21} being approximately 10 dB lower

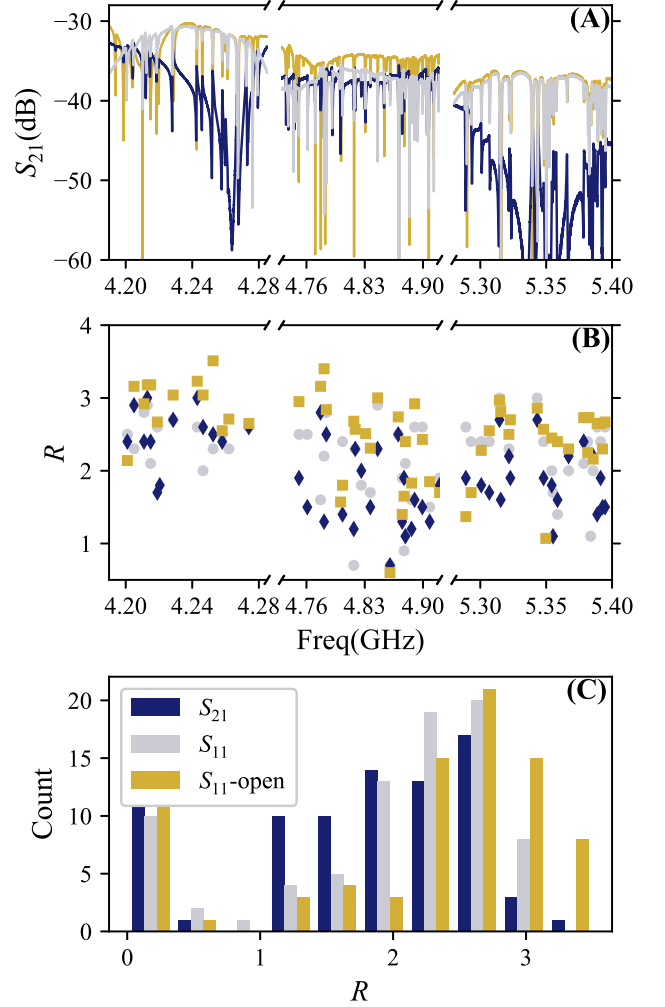


FIG. 5. Comparison of the energy resolution between the S_{11} , S_{21} , and S_{11} -open over a bandwidth of around 100 MHz at 4.19-4.29 GHz, 4.75-4.95 GHz and 5.30-5.40 GHz. (A): The measured amplitude of the S_{11} , S_{21} and S_{11} -open. (B): The measured energy resolution versus frequency. The input power is optimized for each pixel to maximize R . (C): Statistics of R in the measured bands, around 10 pixels in the measured bands, do not show a single photon response.

than that of S_{11} , the measured R from S_{21} remains comparable to S_{11} , while R from S_{11} -Open demonstrates a significant improvement. This trend is consistent for the resonances observed in the 4.75-4.95 GHz and 5.30-5.40 GHz bands.

The statistical analysis of the R s depicted in Fig. 5-(B) is presented in Fig. 5-(C). Notably, the median R is enhanced from 2.0 with S_{21} to 2.6 with S_{11} -Open, and the maximum R reaches approximately 3.5.

The impedance transformation of the readout line, denoted as $(Z_0 + Z_2)$ in Eq. (14), could potentially approach zero, leading to an increase in readout noise as r decreases, as described in Eq. (12) and Eq. (13). To mitigate this issue, one effective approach is to position the resonators at multiples of half wavelength to the open load. Typically, an MKID ar-

ray exhibits resonances between 4 GHz and 8 GHz, with the wavelength of an 8 GHz signal measuring around 16 mm on sapphire. By arranging the pixels within ± 1 mm around the half wavelength, approximately 10 pixels can be accommodated. However, achieving MKIDs in the optical band with resonance frequencies at desired positions presents challenges due to the small size of the pixels. Further investigations are warranted to optimize the performance of MKIDs with a reflection readout scheme. Moreover, it's intriguing to note that despite our MKIDs not being designed to be terminated by an open load, we're observing an increase in the median R -value, suggesting the effectiveness of our method. Additionally, we believe that the proposed readout scheme remains applicable for MKID arrays in the millimeter bands, as indicated by the validity of Eq. (12) and Eq. (13). Even if there's a slight deviation in the resonance frequency from the design, it should still be manageable²⁴.

In conclusion, we have implemented an MKID readout scheme based on reflection. Our observations indicate no significant improvement in the median R when S_{11} is measured together with S_{21} . Adopting a scheme to read out the single-end MKID array yields an enhancement in the median R of the single-end MKID array by 20-30%. This improvement is primarily attributed to the increase in the radius of the resonance circle. It is worth mentioning that this method can also be implemented in systems utilizing superconducting parametric amplifiers^{9,14}.

AVAILABILITY OF DATA

The data supporting the findings of this study are available from the corresponding authors upon reasonable request.

AUTHOR DECLARATIONS

CONFLICT OF INTEREST

The authors have no conflicts to disclose.

ACKNOWLEDGMENTS

The authors would like to thank Shibo Shu from The Institute of High Energy Physics of the Chinese Academy of Sciences for the suggestion for the MKIDs measurement with reflection, as well as Florent Reix, Josiane Firminy, and Thibaut Vacelet from Paris Observatory for assembly and mounting the devices. This work is supported by the European Research Council (ERC) through Grant 835087 (SPIAKID) and the UnivEarthS Labex program.

Appendix A: Reflection of the Resonator with Mis-match

The Z_{in} of the system can be calculated as

$$Z_{in} = Z_1 + \frac{Z_3(Z_2 + Z_0)}{Z_3 + (Z_2 + Z_0)} \quad (S1)$$

The S_{11} can be obtained as

$$S_{11} = \frac{Z_{in} - Z_0}{Z_{in} + Z_0} = \frac{Z_3(Z_1 + Z_2) + (Z_1 - Z_0)(Z_0 + Z_2)}{Z_3(2Z_0 + Z_1 + Z_2) + (Z_0 + Z_1)(Z_0 + Z_2)} \quad (S2)$$

with

$$\hat{Z}_0 = \frac{2(Z_1 + Z_0)(Z_2 + Z_0)}{2Z_0 + Z_1 + Z_2} \quad (S3)$$

Then, S_{11} is

$$S_{11} = \frac{AZ_3 + \Gamma_0}{1 + 2Z_3/\hat{Z}_0} \quad (S4)$$

with

$$A = \frac{Z_1 + Z_2}{(Z_0 + Z_1)(Z_0 + Z_2)} \quad (S5)$$

$$\Gamma_0 = \frac{Z_1 - Z_0}{Z_1 + Z_0} \quad (S6)$$

The S_{21} can be expressed as

$$S_{21} = \frac{2Z_0}{2Z_0 + Z_1 + Z_2} \left(1 - \frac{1}{1 + 2Z_3/\hat{Z}_0}\right) \quad (S7)$$

with

$$\frac{1}{1 + 2Z_3/\hat{Z}_0} = \frac{Q/Q_c - 2jQx_a}{1 + 2jQx_g} \quad (S8)$$

S_{11} can be segmented into two parts as

$$S_{11} = \gamma \left(1 - \frac{1}{1 + 2Z_3/\hat{Z}_0}\right) + \frac{\Gamma_0}{1 + 2Z_3/\hat{Z}_0} \quad (S9)$$

with $\gamma = (Z_1 + Z_2)/(2Z_0 + Z_1 + Z_2)$.

By taking into account of Eq. (S7), Eq. (S9) becomes

$$S_{11} = \frac{Z_1 + Z_2}{2Z_0} S_{21} - \Gamma_0 \frac{Q/Q_c - 2jQx_a}{1 + 2jQx_g} \quad (S10)$$

or

$$S_{11} = \gamma - (\gamma - \Gamma_0) \frac{Q/Q_c - 2jQx_a}{1 + 2jQx_g} \quad (S11)$$

Then, the S_{11} can be fitted with

$$S_{11} = (\gamma - \Gamma_0) \left(\gamma_0 - \frac{Q/Q_c - 2jQx_a}{1 + 2jQx_g}\right) \quad (S12)$$

with $\gamma_0 = \gamma/(\gamma - \Gamma_0)$ as a complex fitting parameter. For the single-end resonator, $Z_2 \rightarrow \infty$ and $\gamma \rightarrow 1$. If the resonator is perfectly matched, $Z_1 = 0$ and $\Gamma_0 = -1$. Thus, S_{11} can be expressed as

$$S_{11} = 1 - 2 \frac{Q/Q_c - 2jQx_a}{1 + 2jQx_g} \quad (S13)$$

which is similar with the expression of S_{11} found in previous publications.

Appendix B: The Coupling Quality Factor and Resonance circle

The coupling quality factor can be calculated as follows. The energy stored in the capacitor and inductor are the same at the resonance frequency, which is

$$E = 2 \times \frac{1}{2} CV^2 \quad (S1)$$

where V is the voltage of the capacitor. The energy dissipated outside the resonator is

$$P = |I|^2 \text{Re}\{R\} \approx \omega^2 C_c^2 V^2 \text{Re}\left\{\frac{(Z_0 + Z_1)(Z_0 + Z_2)}{2Z_0 + Z_1 + Z_2}\right\} \quad (S2)$$

Q_c can then be calculated by definition as

$$Q_c = \omega \frac{E}{P} = \frac{C}{\omega C_c^2} \text{Re}\left\{\frac{2Z_0 + Z_1 + Z_2}{(Z_0 + Z_1)(Z_0 + Z_2)}\right\}. \quad (S3)$$

We compare the radius of the resonance circle between the S_{11} , S_{21} and S_{11} -Open. The term in the bracket of Eq. (S12)

$$S_{11}^b = \gamma_0 - \frac{Q/Q_c - 2jQx_a}{1 + 2jQx_g} \quad (S4)$$

is a circle on the IQ plane. The three points on the resonance circle can be determined as

$$S_{11}^b = \begin{cases} \gamma_0 & x \rightarrow \infty \\ \gamma_0 - Q/Q_c - 2jQx_a & x = 0 \\ \gamma_0 - \frac{Q/Q_c - 2jQx_a}{1 + jQ} & x = 1/2 \end{cases} \quad (S5)$$

Here we assume $\gamma_0 = \gamma_r + j\gamma_i$, then the center of and the radius of the resonance circle is

$$[x_0^b, y_0^b] = [\gamma_r - \frac{Q}{2Q_c}, \gamma_i + 2Qx_a] \quad (S6)$$

$$R_b = \frac{Q}{2Q_c} \sqrt{4(Qcx_a)^2 + 1} \quad (S7)$$

Taking into account of the coefficients, the radius of the resonator circle of the S_{11} is

$$R_r = |\gamma_{21} - \Gamma_0| \frac{Q}{2Q_c} \sqrt{4(Qcx_a)^2 + 1} \quad (S8)$$

If the resonator is perfectly matched, $\gamma_{21} = 0$. $\Gamma_0 = -1$. In the case that the $Z_2 \rightarrow \infty$, which is the case that the MKIDS is terminated with an open load. $\gamma_{21} = 1$ In the case

$$R_r = \begin{cases} \frac{Q_i}{2(Q_i + Q_c)} \sqrt{4(Qcx_a)^2 + 1} & Z_1 = 0 \text{ \& } Z_2 = 0 \\ \frac{Q_i}{Q_i + Q_c} \sqrt{4(Qcx_a)^2 + 1} & Z_1 = 0 \text{ \& } Z_2 = \infty \end{cases} \quad (S9)$$

with $1/Q = 1/Q_i + 1/Q_c$. Thus, there is an increase of a factor of 2 in the resonator terminated with an open load. Similarly, the radius of S_{21}

$$R_t = \left| \frac{2Z_0}{2Z_0 + Z_1 + Z_2} \right| \frac{Q}{2Q_c} \sqrt{4(Qcx_a)^2 + 1} \quad (S10)$$

In the situation that $Z_1 = Z_2 = 0$,

$$R_t = \frac{Q_i}{2(Q_i + Q_c)} \sqrt{4(Qcx_a)^2 + 1} \quad (S11)$$

¹P. K. Day, H. G. LeDuc, B. A. Mazin, A. Vayonakis, and J. Zmuidzinias, *Nature* **425**, 817 (2003).

²Adam, R., Adane, A., Ade, P. A. R., André, P., Andrianasolo, A., Aussel, H., Beelen, A., Benoît, A., Bideaud, A., Billot, N., Bourrion, O., Bracco, A., Calvo, M., Catalano, A., Coiffard, G., Comis, B., De Petris, M., Désert, F.-X., Doyle, S., Driessen, E. F. C., Evans, R., Goupy, J., Kramer, C., Lagache, G., Leclercq, S., Leggeri, J.-P., Lestrade, J.-F., Macías-Pérez, J. F., Mauskopf, P., Mayet, F., Maury, A., Monfardini, A., Navarro, S., Pascale, E., Perotto, L., Pisano, G., Ponthieu, N., Revéret, V., Rigby, A., Ritacco, A., Romero, C., Roussel, H., Ruppig, F., Schuster, K., Sievers, A., Trique-neaux, S., Tucker, C., and Zylka, R., *A&A* **609**, A115 (2018).

³S. R. Meeker, B. A. Mazin, A. B. Walter, P. Strader, N. Fruitwala, C. Bockstiegel, P. Szypryt, G. Ulbricht, G. Coiffard, B. Bumble, G. Cancelo, T. Zmuda, K. Treptow, N. Wilcer, G. Collura, R. Dodkins, I. Lipartito, N. Zobrist, M. Bottom, J. C. Shelton, D. Mawet, J. C. van Eyken, G. Vasisht, and E. Serabyn, *Publications of the Astronomical Society of the Pacific* **130**, 065001 (2018).

⁴H. Jie, N. Paul, B. Faouzi, M. Jean-Marc, C. Christine, M. Alexine, R. Florent, F. Josiane, V. Thibaut, P. V. Dung, P. Michel, C. Elisabetta, and B. Piercarlo, *Journal of Low Temperature Physics* (2023), 10.1007/s10909-023-03018-5.

⁵N. J. Swimmer, Ph. d thesis, University of California, Santa Barbara (2023).

⁶B. A. Mazin, B. Bumble, S. R. Meeker, K. O'Brien, S. Mchugh, and E. Langman, *Optics Express* **20**, 1503 (2012).

⁷J. Gao, M. R. Vissers, M. O. Sandberg, F. C. S. da Silva, S. W. Nam, D. P. Pappas, D. S. Wisbey, E. C. Langman, S. R. Meeker, B. A. Mazin, H. G. Leduc, J. Zmuidzinias, and K. D. Irwin, *Applied Physics Letters* **101**, 142602 (2012).

⁸P. J. de Visser, S. A. de Rooij, V. Murugesan, D. J. Thoen, and J. J. Baselmans, *Phys. Rev. Applied* **16**, 034051 (2021).

⁹N. Zobrist, W. H. Clay, G. Coiffard, M. Daal, N. Swimmer, P. Day, and B. A. Mazin, *Physical Review Letters* **129**, 017701 (2022).

¹⁰S. Beldi, F. Boussaha, J. Hu, A. Monfardini, A. Traini, F. Levy-Bertrand, C. Chaumont, M. Gonzales, J. Firminy, F. Reix, M. Rosticher, S. Mignot, M. Piat, and P. Bonifacio, *Opt Express* **27**, 13319 (2019).

¹¹J. Hu, F. Boussaha, J.-M. Martin, P. Nicaise, C. Chaumont, S. Beldi, M. Piat, and P. Bonifacio, *Applied Physics Letters* **119** (2021), 10.1063/5.0074103.

¹²P. Nicaise, J. Hu, J.-M. Martin, S. Beldi, C. Chaumont, P. Bonifacio, M. Piat, H. Geoffray, and F. Boussaha, *Journal of Low Temperature Physics* **209**, 1242 (2022).

¹³J. Gao, J. Zmuidzinias, A. Vayonakis, P. Day, B. Mazin, and H. Leduc, *Journal of Low Temperature Physics* **151**, 557 (2008).

¹⁴N. Zobrist, G. Coiffard, B. Bumble, N. Swimmer, S. Steiger, M. Daal, G. Collura, A. B. Walter, C. Bockstiegel, N. Fruitwala, I. Lipartito, and B. A. Mazin, *Applied Physics Letters* **115**, 213503 (2019).

¹⁵C. Wang, Y. Y. Gao, I. M. Pop, U. Vool, C. Axline, T. Brecht, R. W. Heeres, L. Frunzio, M. H. Devoret, G. Catelani, L. I. Glazman, and R. J. Schoelkopf, *Nat Commun* **5**, 5836 (2014).

¹⁶H. Wang, S. Singh, C. R. H. McRae, J. C. Bardin, S. X. Lin, N. Messaoudi, A. R. Castelli, Y. J. Rosen, E. T. Holland, and D. P. Pappas, *Quantum Science and Technology* **6**, 035015 (2021).

¹⁷M. S. Khalil, M. J. A. Stoutimore, F. C. Wellstood, and K. D. Osborn, *Journal of Applied Physics* **111**, 054510 (2012).

¹⁸J. Baselmans, S. Yates, P. Diener, and P. de Visser, *Journal of Low Temperature Physics* **167**, 360 (2012).

¹⁹R. Mezzena, M. Faverzani, E. Ferri, A. Giachero, B. Margesin, A. Nucciotti, A. Puiu, and A. Vinante, *Journal of Low Temperature Physics* **199**, 73 (2019).

²⁰R. BARENDS, Ph. d thesis, Tu Delft (2009).

²¹S. R. Meeker, Doctor thesis, University of California Santa Barbara (2017).

²²J. J. A. Baselmans, J. Bueno, S. J. C. Yates, O. Yurduseven, N. Llombart, K. Karatsu, A. M. Baryshev, L. Ferrari, A. Endo, D. J. Thoen, P. J. de Visser,

- R. M. J. Janssen, V. Murugesan, E. F. C. Driessen, G. Coiffard, J. Martin-Pintado, P. Hargrave, and M. Griffin, *Astronomy & Astrophysics* **601**, A89 (2017).
- ²³S. Shibo, M. Calvo, J. Goupy, S. Leclercq, A. Catalano, A. Bideaud, A. Monfardini, and E. F. C. Driessen, *Applied Physics Letters* **113**, 082603 (2018).
- ²⁴S. Shu, M. Calvo, J. Goupy, S. Leclercq, A. Catalano, A. Bideaud, A. Monfardini, and E. F. C. Driessen, *Applied Physics Letters* **119** (2021), 10.1063/5.0058335.